

Research



Cite this article: Bousquet GD, Triantafyllou MS, Slotine J-JE. 2017 Optimal dynamic soaring consists of successive shallow arcs. *J. R. Soc. Interface* **14**: 20170496. <http://dx.doi.org/10.1098/rsif.2017.0496>

Received: 10 July 2017
Accepted: 11 September 2017

Subject Category:
Life Sciences – Physics interface

Subject Areas:
biomathematics, biophysics

Keywords:
dynamic soaring, soaring, albatross, trajectory optimization, wind, energy

Author for correspondence:
Gabriel D. Bousquet
e-mail: g_b@mit.edu

Electronic supplementary material is available online at <https://dx.doi.org/10.6084/m9.figshare.c.3887821>.

Optimal dynamic soaring consists of successive shallow arcs

Gabriel D. Bousquet, Michael S. Triantafyllou and Jean-Jacques E. Slotine

Department of Mechanical Engineering, Massachusetts Institute of Technology, Cambridge, MA 02139, USA

GDB, 0000-0003-2008-4793

Albatrosses can travel a thousand kilometres daily over the oceans. They extract their propulsive energy from horizontal wind shears with a flight strategy called dynamic soaring. While thermal soaring, exploited by birds of prey and sports gliders, consists of simply remaining in updrafts, extracting energy from horizontal winds necessitates redistributing momentum across the wind shear layer, by means of an intricate and dynamic flight manoeuvre. Dynamic soaring has been described as a sequence of half-turns connecting upwind climbs and downwind dives through the surface shear layer. Here, we investigate the optimal (minimum-wind) flight trajectory, with a combined numerical and analytic methodology. We show that contrary to current thinking, but consistent with GPS recordings of albatrosses, when the shear layer is thin the optimal trajectory is composed of small-angle, large-radius arcs. Essentially, the albatross is a flying sailboat, sequentially acting as sail and keel, and is most efficient when remaining crosswind at all times. Our analysis constitutes a general framework for dynamic soaring and more broadly energy extraction in complex winds. It is geared to improve the characterization of pelagic birds flight dynamics and habitat, and could enable the development of a robotic albatross that could travel with a virtually infinite range.

1. Introduction

Dynamic soaring is the flight technique where a glider, either a bird or a machine, extracts its propulsive energy from non-uniform horizontal winds such as those found over the oceans. Wandering albatrosses (*Diomedea exulans*), the archetypal dynamic soarers, have been recorded to travel 5000 km per week while relying on wind energy alone [1–3]. The engineering potentialities of dynamic soaring are tantalizing: a robotic albatross could survey the oceans (or ride the wind shear of jet streams [4]), and collect oceanic and atmospheric data, travelling at over 40 knots with a virtually infinite range [5,6].

A major obstacle to intelligent robotic soaring resides in the complexity of the wind power extraction process that, by nature, requires planning on-the-go an energy positive trajectory in a stochastic, hard to measure, and poorly understood wind field. Conversely, progress in the description of dynamic soaring energetics can help design efficient algorithmic solutions to the online trajectory planning problem. Improving the understanding of dynamic soaring is also important in avian ecology. In particular, it enables better evaluation of the impact of climate change on the behaviour and habitat of albatrosses, petrels and other pelagic birds, that are dependent on specific wind conditions [7].

At the mesoscale, it is known that the vast majority of the wandering albatross' flight is performed in an overall cross- or downwind direction, by dynamic soaring [3]. Although on relatively rare occasions (attributed to foraging [8]), they may fly upwind, in those instances they typically need to provide propulsive power. As far as dynamic soaring is concerned, crosswind flight (i.e. when the average airspeed is orthogonal to the average wind direction) is the dominant mode, and the focus of this paper.

In the first attempt to describe dynamic soaring, Rayleigh [9] modelled the wind profile (figure 1) as a still boundary layer separated from the above windy free stream blowing at W_0 by an infinitely thin shear layer (figure 1c,

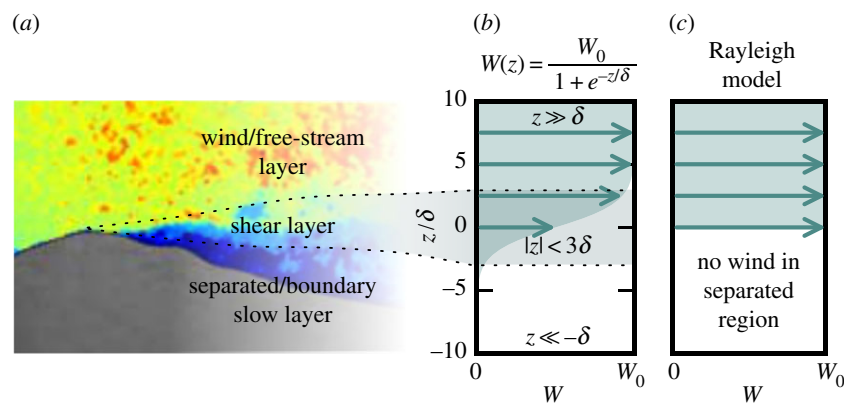


Figure 1. Wind profile. (a) Wind field behind waves. Colour-coding: wind intensity, experimental data adapted from [10]. (b) The logistic wind profile in this study captures adequately the wind field in separated regions, such as behind ocean waves. More generally, it constitutes a robust way to approximate a wide class of wind fields, based on two parameters: a typical wind speed inhomogeneity W_0 separated by a shear layer of typical length-scale δ . (c) Rayleigh's wind model is the limit of the logistic profile for $\delta \rightarrow 0$.

hereafter Rayleigh's wind model). Rayleigh noticed that when traversing the shear layer up- or downwind, the albatross' groundspeed is conserved but its airspeed may increase by up to W_0 . Rayleigh connected up- and downwind transitions with 180° half-turns in order to construct an energy neutral trajectory (hereafter Rayleigh's cycle, figure 2b and e.g. [12]): at each transition, the airspeed gain compensates for the inherent losses due to drag. Because the drag is quadratic with airspeed, a limit cycle is reached. This description of the dynamic soaring trajectory, based on phases of flight directly up- or downwind connected by half-turns, has carried on until today [12–23] in two energetically equivalent forms: trajectories with constant turn direction are O-shaped, or loitering; trajectories with alternating turn directions are S-shaped, or travelling.

Recently published observations based on high-accuracy GPS measurements [1,11,24] (reproduced in figures 2a and 3) show that albatrosses in crosswind flight do not follow half-turns, but rather an elongated, albeit oscillating, trajectory. As we report below, analysis of these data shows that they typically turn by only 50° – 70° , about a third of the Rayleigh cycle's 180° half-turn.

The aim of this paper is to build a model of dynamic soaring that addresses the threefold factor discrepancy in turn amplitude between the half-turn explanation and published field data of flying albatrosses. To this end, we computed the 'minimum-wind trajectory', i.e. the most efficient trajectory of dynamic soaring in the sense that it requires the least amount of wind to allow sustained flight, and we investigated the variation of its shape with the thickness of the shear layer. We discovered that contrary to prevailing theory, the most efficient trajectory in the thin shear layer regime is a sequence of arcs of vanishingly small angle, with the direction of flight nearly crosswind at all times. We were able to explain this observation analytically, lowering the wind required for dynamic soaring by over 35% compared to previous models [5].

2. Material and methods

2.1. Wind model

In the last two decades, a popular approach has consisted of pursuing accurate numerical modelling of albatross flight in logarithmic or power-law wind profiles, deemed good models of the

average wind field in the first 20 m above water, where the albatross flies. However, in this framework it has been shown [25,26] that dynamic soaring is extremely sensitive to the wind field in the first metre above the surface, precisely where wind–wave interactions and temporal variability make the logarithmic model less relevant.

By contrast, Rayleigh's discontinuous wind model embraces the sharp wind shear that exists in separated regions, such as behind breaking waves or mountain ridges. Recent studies suggest that wind separation in ocean wave fields may be more frequent than previously believed ([10] and figure 1a), further reducing the relative merit of log-based descriptions.

In this study, rather than attempting to conduct high-fidelity, high-complexity modelling of dynamic soaring for a specific system, we aim for a general and robust analysis of the principles of dynamic soaring, the main conclusions of which should hold independently of the details of the wind field or glider. This approach is in part motivated by the fact that despite the significant stochasticity of the wind field in which albatrosses fly, their trajectory is quite regular. With this in mind, the wind profile, which varies with altitude z , is modelled by means of a logistic function (figure 1b) parameterized by the free stream wind speed W_0 and the shear layer thickness parameter δ

$$W(z) = \frac{W_0}{1 + \exp(-z/\delta)}. \quad (2.1)$$

This formulation, also suggested in [22] for modelling the wind field behind ridges, is intended to capture not only the main features of separated winds over ocean waves (see [12,27,28] for a qualitative discussion), but also more generally any flow with a typical wind inhomogeneity W_0 developing over a typical length-scale δ , such as in turbulence soaring [29,30]. The regions of $z \ll -\delta$, $|z| \lesssim 3\delta$, $z \gg \delta$ represent a slow layer (separated region or boundary layer), shear layer of typical thickness $\Delta = 6\delta$, and windy free-stream layer, respectively. In the thin shear layer limit $\delta \rightarrow 0$ the model converges to Rayleigh's.

In a logarithmic profile (used to model attached flows), the boundary layer is both the slow layer and the shear layer. An assumption of our approach is that even logarithmic profiles have a characteristic shear layer thickness δ and a characteristic wind intensity W_0 such that equation (2.1) may be used to approximately represent those flows as well.

2.2. Equations of motion

We use a 3-degree-of-freedom model to represent the flight of an albatross or glider in a wind shear. Our formulation follows closely [5,31] in the frame of reference $(\mathbf{i}, \mathbf{j}, \mathbf{k}) = (\mathbf{e}_{\text{East}}, \mathbf{e}_{\text{North}}, \mathbf{e}_{\text{Down}})$.

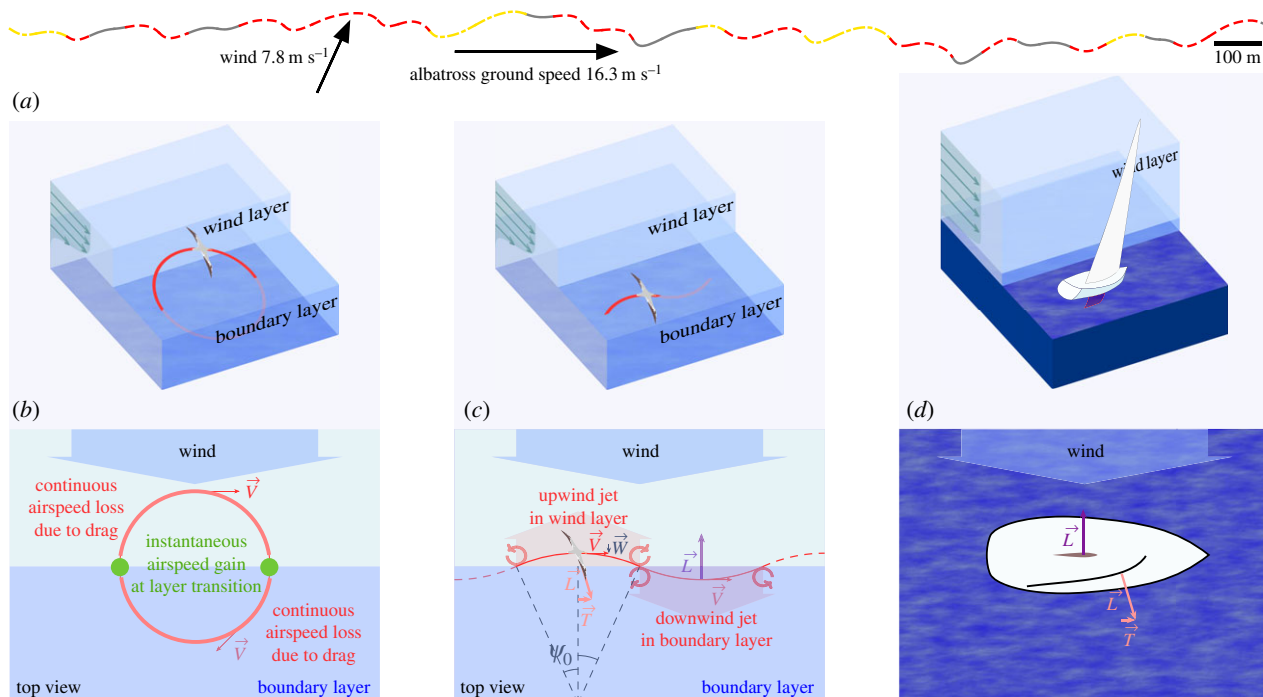


Figure 2. The albatross' trajectory. (a) Recording of a flying albatross from [11] (top view). In crosswind flight the typical turn of the albatross is approximately $50^\circ - 70^\circ$. Dot-dashed yellow portions of the trajectory: the albatross is involved in a 60° turn within $\pm 20^\circ$. Dashed red portions: the albatross is involved in a 60° turn within $\pm 10^\circ$. Note that while in the ground frame the mean albatross travel has a downwind component, in the frame moving with the average wind it is nearly crosswind. (b) Rayleigh cycle describes the albatross' flight as a sequence of half-turns between the windy and slow regions. At each layer transition, there is an airspeed gain equal to the wind speed, which compensates inherent drag losses that are quadratic in airspeed. However, this trajectory is suboptimal for energy extraction. Instead, for thin shear layers, the optimal cycle (c) is composed of a succession of small-angle arcs. The flight portion in the wind layer is functionally analogous to the sail of a sailboat, while the portion in the slow layer is analogous to the keel of a sailboat (d).

\mathbf{e}_{UP}). Within this framework, six parameters fully define the glider's state: $\mathbf{x} = (V, \psi, \gamma, z, x, y)$. Here, V is the glider airspeed, and ψ and γ are the air-relative heading angle and air-relative flight path angle, respectively. Specifically, ψ is the angle between \mathbf{i} and the projection of the airspeed vector \mathbf{V} in the \mathbf{ij} -plane and γ is the angle between \mathbf{V} and the \mathbf{ij} -plane and is positive nose up. We assume that the wind is blowing from north to south when $W > 0$, i.e. $\mathbf{W}(z) = -W(z)\mathbf{j}$. The control inputs are the lift coefficient and roll angle $\mathbf{u} = (c_L, \phi)$.

The equations of motion (EOM) are

$$m\dot{V} = -D - mg \sin \gamma + m\dot{W} \cos \gamma \sin \psi, \quad (2.2a)$$

$$mV\dot{\gamma} = L \cos \phi - mg \cos \gamma - m\dot{W} \sin \gamma \sin \psi, \quad (2.2b)$$

$$mV\dot{\psi} \cos \gamma = L \sin \phi + m\dot{W} \cos \psi, \quad (2.2c)$$

$$\dot{z} = V \sin \gamma, \quad (2.2d)$$

$$\dot{x} = V \cos \gamma \cos \psi, \quad (2.2e)$$

$$\text{and} \quad \dot{y} = V \cos \gamma \sin \psi - W, \quad (2.2f)$$

where the dots represent time derivation $\dot{V} = dV/dt$ and so on. Note that x, y in equations (2.2e) and (2.2f) may be considered as *outputs* rather than *states* as they do not feed back into the self-contained dynamics of equations (2.2a)–(2.2d). Following standard quasi-steady flight dynamics theory, lift and drag are specified according to $L = 1/2 c_L \rho S V^2$ and $D = 1/2 c_D \rho S V^2$. We assume quadratic drag $c_D = c_{D,0} + k c_L^2$. The coefficient $c_{D,0}$ represents the system's drag when no lift is generated and the parameter k expresses the additional generation of drag due to lift. Denoting $f \equiv c_L/c_D$ the glider's lift-to-drag ratio (or *fineness*), k is related to the maximum lift-to-drag ratio by $k^{-1} = 4f_{\max}^2 c_{D,0}$. For the numerical analysis below, $c_{D,0}$ and k are chosen such that the maximum lift-to-drag ratio f_{\max} is reached at a lift coefficient of maximum glide ratio $c_{L,f_{\max}} = 0.5$, typical of a small glider.

2.3. Non-dimensionalization

To compute the EOM numerically, and to obtain scale-invariant results, it is useful to rewrite equation (2.2) in non-dimensional form. For that purpose, the velocities are renormalized by the glider's

characteristic speed at $c_L = 1$, namely $V_c = \sqrt{mg/(\frac{1}{2}\rho S)}$. The distances are renormalized by the characteristic length $\lambda = (V_c)^2/g$. Finally, time is renormalized by the timescale $t_c = V_c/g = \lambda/V_c$. Note that our non-dimensionalization depends only on the glider properties, air density, and gravity, arguably a more natural choice than approaches based on the wind gradient [31].

The speed V_c , directly related to the notion of 'wing loading' (ratio between mass and wing area) expresses the order of magnitude of the airspeed at which the glider naturally flies. For instance, for a wandering albatross, $V_c = 15 \text{ m s}^{-1}$ (see §2.5). Similarly, the length λ expresses what is a 'small' or 'large' change in altitude. For an albatross, $\lambda = 24 \text{ m}$ so a change of altitude of $2.4 \text{ m} \ll \lambda$ is 'small' but a change of altitude of $240 \text{ m} \gg \lambda$ is 'large'. For a cruising A380 large passenger aircraft, $\lambda_{A380} = 2.3 \text{ km}$ so an altitude change of 230 m is 'small' but a change of altitude of 23 km is 'large'.

Upon non-dimensionalization of the variables $v = V/V_c$, $w = W/V_c$, $\tilde{x} = x/\lambda$, $\tilde{y} = y/\lambda$, $\tilde{z} = z/\lambda$, $\tau = t/t_c$ and $(\cdot)' = d(\cdot)/d\tau$, equation (2.2) becomes

$$v' = -c_D v^2 - \sin \gamma + w' \cos \gamma \sin \psi, \quad (2.3a)$$

$$v\gamma' = c_L v^2 \cos \phi - \cos \gamma - w' \sin \gamma \sin \psi, \quad (2.3b)$$

$$v \cos \gamma \psi' = c_L v^2 \sin \phi + w' \cos \psi, \quad (2.3c)$$

$$\tilde{z}' = v \sin \gamma, \quad (2.3d)$$

$$w' = \frac{\partial w}{\partial \tilde{z}} \tilde{z}', \quad (2.3e)$$

$$\tilde{x}' = v \cos \gamma \cos \psi \quad (2.3f)$$

$$\text{and} \quad \tilde{y}' = v \cos \gamma \sin \psi - w. \quad (2.3g)$$

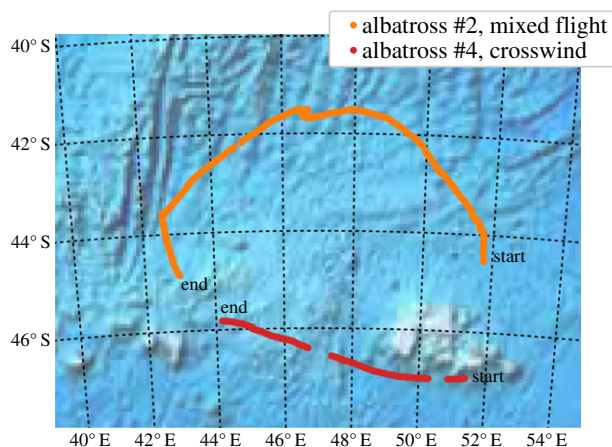


Figure 3. Wandering albatrosses #2 and #4 from Yonehara *et al.* [24], analysed in this study. The track of albatross #2 is over 1700-km-long, lasts for approximately 2 days and is made of up-, cross- and downwind flights in low and high winds, separated by active foraging and resting periods. The track of albatross #4 is a nearly uninterrupted, 650 km, 9 h, approximately crosswind flight performed in $8\text{--}15\text{ m s}^{-1}$ winds. Note that some data are missing or dropped due to poor GPS quality.

The non-dimensionalization does not depend on the glider's characteristics except through the lift-drag coefficient curve $c_L \mapsto c_D$. For the remainder of this manuscript when there is no ambiguity the \sim signs are omitted for notational simplicity.

2.4. Numerical trajectory optimization

A direct collocation method is applied to equation (2.3) with the wind model of equation (2.1), in order to compute the minimum-wind trajectory of dynamic soaring. Specifically, the aim is to find the minimum wind needed to sustain flight, i.e. the algorithm searches for the minimum wind intensity w_0 such that equation (2.3) has a solution periodic in $(v, \gamma, \psi + 2p\pi, z)$ with $p = 0, \pm 1$. More details on the procedure can be found in electronic supplementary material, ST1 and e.g. [5,25,31]. The optimal loitering ($p = \pm 1$) and travelling trajectories ($p = 0$) are computed for several values of the shear layer thickness parameter δ , starting from a thick shear layer ($\delta \gg \lambda$) and reducing δ progressively until the thin shear layer regime ($\delta \ll \lambda$) is reached. The resulting trajectories are displayed in figure 4.

2.5. Dimensions for the wandering albatross' flight

Upon non-dimensionalization in §2.3, the trajectories that satisfy equation (2.3) are scale-independent. With the quantities below they may be rescaled to represent the conditions of the albatross' flight.

2.5.1. Albatross properties

The typical properties for the wandering albatross are collected in table 1, and are used to convert the results of §2.4 and the analytic analysis below back into dimensional form. Further information on mass and wing area of wandering albatrosses may be found in e.g. [7,32]. To the best of our knowledge, the coefficient of minimum power $(c_L^{3/2}/c_D)_{\max}$, which is the important aerodynamic property for dynamic soaring ability in light winds as shown in equation (3.7) below, has not been specifically studied for the wandering albatross. For this study the numerical value 22 is chosen. It is similar to the 19.6 value from [5,25], which is based on the simulation of a glider with size and plan-form similar to that of wandering albatrosses. It is also similar to

the 22.9 value obtained by evaluating the quadratic drag formulation of [33] at a lift coefficient $c_L = 1.25$. Overall, we estimate the uncertainty over this coefficient to be approximately 10%, comparable to that of mass and wing area.

2.5.2. Wind properties

The wind parameters δ and W_0 are more uncertain than the albatross' properties because the wind structure depends on the sea state, is complex and time-varying, and is poorly known overall.

The effective shear layer thickness perceived by the albatross must be at least of the order of the vertical distance from wingtip to wingtip when the albatross is in a roll. Given the wandering albatross' 3 m span, the perceived shear layer must be thicker than approximately 1 m. In the presence of large waves, Pennycuik's description of dynamic soaring as 'gust soaring' at the interface between windy and separated regions behind waves [27] is indicative of a thin shear layer, of size comparable to the albatross'. Accordingly, observational data of flying albatrosses suggest a shear layer thickness of the order of 1–3 m in the presence of waves. Conversely, when the waves are small and the wind flow remains attached to the surface, it is possible that the albatross does not have access to the extremely thin boundary layer and as a consequence perceives a virtually thicker shear layer. For logarithmic profiles, the perceived shear layer thickness would be approximately 7 m (see electronic supplementary material, ST3). It is also possible to estimate the shear layer thickness indirectly from vertical travel reports of soaring albatrosses. The literature [1,11,27] suggests that over a dynamic soaring cycle, the albatross travels vertically by 5–15 m. The results of the numerical analysis of §2.4 show that for the minimum-wind trajectory there is a correlation between vertical travel and shear layer thickness. Referring to figure 7a, such vertical travels correspond to a shear layer thickness of approximately 1.5–7 m (3 m thickness for the 8 m vertical travel reported in [27]). Overall, considerations on separation behind waves, the albatross size and albatross' vertical travel suggest a shear layer thickness of the order of 1–3 m (in this study, we select 2 m as the default thickness), at the very maximum 7 m.

The intensity parameter W_0 in equation (2.1) does not necessarily denote the wind speed *stricto sensu*, but more precisely the speed difference between the fast and slow layers. For instance, the 7.8 m s^{-1} wind reported in figure 2a is the wind at 10 m (see [11]). The speed of the slow layer is non-zero, as even behind separated waves, the mass of air typically travels at the wave phase speed [34]. Accordingly, the albatross can only exploit a fraction of the wind speed. Similarly, in non-separated flows the low-height wind at 1 m is typically more than 50% of the wind at 10 m and here again, only a relatively small fraction of the wind speed can be exploited [25]. In the present study, we assume that the albatross may access 25–50% of the wind speed at 10 m.

2.6. Analysis of flight data from the literature

For wandering albatrosses in crosswind, the typical dynamic soaring manoeuvre lasts for 5–15 s and extends over 50–150 m, such that analysing the albatross' flight at the cycle level requires measuring its trajectory at a sampling rate of 1 Hz or more. The present study reanalyses a short (3 km) track from Sachs *et al.* [11] with a high (10 Hz) sampling rate, and two long (order of 1000 km) tracks from Yonehara *et al.* [24] sampled at a lower rate (1 Hz). Sachs' track [11] contains 20 soaring cycles while Yonehara's tracks [24] contains thousands of them. For each recording, characteristics of the flight are computed,

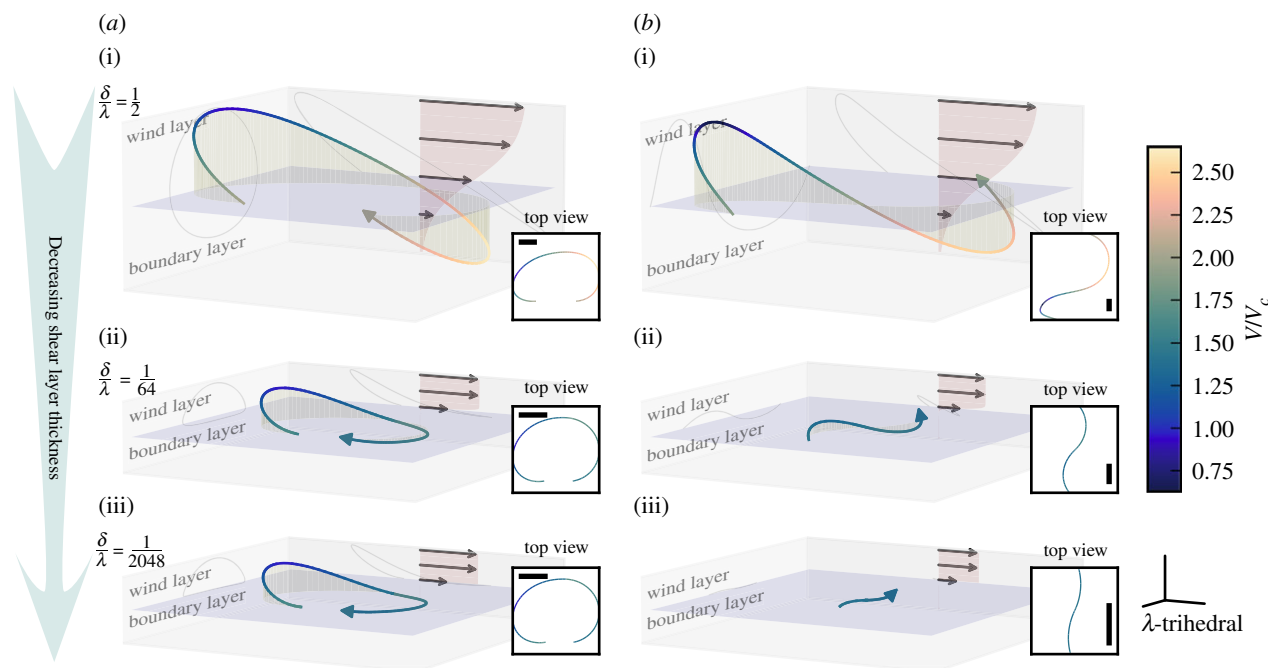


Figure 4. Minimum wind trajectories for three shear layer thicknesses (see the wind profiles in the plots' backgrounds and how they relate to shear layer thickness in figure 1). (a) The trajectories are constrained to fulfil the specific requirement that the heading increases by 360° over a cycle, hence their loitering appearance. (b) The heading is required to be periodic, hence their travelling appearance. For the three-dimensional trajectories the scale is common and is indicated on the bottom right corner: the trihedral is of length $\lambda = 2m/(\rho S)$ (24 m for an albatross). The scale bars on the top view insets are of length λ . a(ii), b(ii) $\delta/\lambda = \frac{1}{64}$ are representative of the shear layer thickness experienced by albatrosses. The travelling trajectory requires less wind than the loitering one, with an increasing advantage for thinner shear layers. When $\delta/\lambda \rightarrow 0$, the travelling trajectory becomes two-dimensional and is composed of a sequence of vanishingly small arcs of finite curvature performed at nearly constant speed. The behaviour of the loitering trajectory is qualitatively different: for decreasing shear layer thicknesses, it quickly converges to a limit trajectory that remains significantly three-dimensional even for an infinitely thin shear layer.

e.g. cycle turn amplitude (see electronic supplementary material, ST2 for more details on the procedure).

2.6.1. Albatross track

The albatross track in Sachs *et al.* [11], reproduced in figure 2a, has two characteristics that make it well-suited for the present study: (i) the high sampling rate allows for reliable measurements of the small-scale features of individual turns and (ii) the wind intensity, reported at $7.8 \pm 2 \text{ m s}^{-1}$ (see [11] and reference herein for methodology of determining the wind from satellite measurements), lies at the lower end of the wandering albatross' dynamic soaring flight envelope.

In this study, we discuss the dynamic soaring trajectory that minimizes the required wind. In practice, a flying albatross fulfils more complex objectives, for instance foraging, which may involve sub-objectives such as minimizing control effort, selecting cross-country average speed direction and altitude, etc. In particular, when the wind is plentiful, staying aloft is comparatively easy and it is less likely that the albatross' objective is to extract as much energy as possible. When the wind is weak however, it is likely that staying aloft becomes the albatross' main objective, as in our model. Accordingly, the low-wind of [11] is valuable as in it the albatross must pursue an objective similar to our computations. In the 20-cycle (40-turn) recording, the albatross' median turn is 54° (mean 50°), with a standard deviation of 21° (figures 2 and 6; electronic supplementary material, ST2).

2.6.2. Albatross tracks

Two recordings of wandering albatrosses from Yonehara *et al.* [24,35] are reproduced in figure 3. Over the course of 2 days, albatross #2 performs 'mixed' flights made of up-, cross- and downwind flights in low and high winds, separated by active foraging and resting periods. It has over 1700 km of usable flight data and over 13 000 turns. Albatross #4 contains a

nearly uninterrupted, generally westwards flight. In [35], the wind is measured with satellite data and estimated from the albatross track itself. Both methods suggest that overall the flight is approximately crosswind, in $8\text{--}15 \text{ m s}^{-1}$ winds. It has 650 km of usable data in 3700 turns, performed over the span of 9 h. The median turn for albatross #2 in mixed flight is 78° (mean 84° , s.d. 46°). The median turn for albatross #4 in crosswind flight is 66° (mean 69° , s.d. 32°) (figure 6; electronic supplementary material, ST2. For more details on the open-access dataset [24] and the in-flight wind conditions, see the electronic supplementary materials of [35]).

3. Results

3.1. Three-dimensional minimum-wind trajectories in a logistic wind profile

Figure 4 shows the minimum-wind trajectory for three shear layer thicknesses (thick, albatross-like conditions and thin). The main attributes of the cycle, spanning several orders of magnitude in shear layer thickness from $\delta \ll \lambda$ to $\delta \gg \lambda$ are displayed in figures 6 and 7.

When the shear layer is thick all trajectories are significantly three-dimensional, the loitering and travelling trajectories are quantitatively similar, and the turn amplitude of the travelling trajectory is large. When the shear layer is thin however the loitering and travelling trajectories are distinctly different. While the loitering trajectory remains significantly three-dimensional, the travelling trajectory's extension in the z -direction shrinks and it becomes nearly two-dimensional. As the shear layer thickness parameter δ is decreased, the trajectory becomes more and more

Table 1. Characteristics of the albatross used in this study. λ and V_c are calculated with the air density $\rho = 1.2 \text{ kg m}^{-3}$ and acceleration of gravity $g = 9.8 \text{ m s}^{-2}$.

mass m (kg)	9.5
wing area S (m^2)	0.65
minimum power coefficient $(c_L^{3/2}/c_D)_{\max}$	22
λ (m)	24.3
V_c (m s^{-1})	15.5

elongated, and is composed of zigzags of only a few degrees in amplitude (figure 6b). Importantly, it requires only approximately two-thirds as much wind as the loitering trajectory (figure 6a).

3.2. Analytic solution in the thin shear layer regime

When the shear layer is thin $\delta \ll \lambda$, the logistic wind profile resembles Rayleigh's. As observed in the numerical analysis, the travelling trajectory is approximately two-dimensional and remains in the neighbourhood of $z = 0$. This property greatly reduces the problem complexity and it is possible to build a quantitatively accurate analytic solution in this limit of a very thin shear layer.

The cycle may be decomposed into two parts: first, glide phases on either side of, but close to, the shear layer ($\delta \ll |z| \ll \lambda$) where the wind shear is weak and airspeed is lost due to drag, and secondly, transitions across $z = 0$ of vanishing duration but finite impulse where airspeed gain takes place.

3.2.1. Glide

Consider the dynamics of a glider evolving according to equation (2.3) in the vicinity $z = 0^\pm$ of the separating plane but not crossing the separation layer. The two-dimensional approximation $z = 0^\pm$ brings $\gamma, \gamma' = 0$. Equation (2.3b) becomes a constraint on the roll angle $\cos \phi = 1/c_L v^2$ and equation (2.3) simplifies to

$$v' = -c_D v^2 \quad (3.1a)$$

and

$$\psi' = c_L v \sin \phi. \quad (3.1b)$$

Eliminating τ , the parametric evolution of v follows:

$$\frac{dv}{d\psi} = -\frac{1}{f} \frac{v}{\sqrt{1 - 1/(c_L^2 v^4)}} \cdot \text{sign}(\psi'), \quad (3.2)$$

reflecting the airspeed cost of turning. The sign function is a consequence of the decrease of airspeed with time regardless of whether the turn is to port or starboard.

3.2.2. Layer transition

Within the thin shear layer, the wind profile can be approximated by a step function $w(z) = H(z)w_0$. The Heavyside step function $H(z)$ is 0 if $z < 0$ and 1 if $z > 0$. The time derivative of the local wind seen by the glider in equation (2.3e) becomes $w' = w_0 \delta(z)z'$, where $\delta(z)$ is the Dirac distribution. This discontinuity in the EOM induces a finite change of the glider's state. The state transition $(\psi_-, v_-) \mapsto (\psi_+, v_+)$

can be easily computed from groundspeed continuity (a consequence of the forces remaining finite). In airspeed quantities it is expressed as $\mathbf{V}^+ = \mathbf{V}^- + W\mathbf{j}$ depending on whether the transition is up or down. This leads to

$$\tan \psi^+ = \tan \psi^- \pm \frac{w_0}{v^- \cos \psi^-} \quad (3.3a)$$

and

$$v^+ = v^- \sqrt{1 \pm \frac{2w_0}{v^- \sin \psi^-} + \left(\frac{w_0}{v^-}\right)^2}. \quad (3.3b)$$

Note that equation (3.3a) is also smooth near $\psi = \pm \pi/2$. Note also that while the state (ψ^+, v^+) and (ψ^-, v^-) are taken on both sides of the shear layer, the formulae are also valid for intermediate locations within the shear layer itself. For instance, the state (ψ_0, v_0) in the middle of the shear layer $z = 0$ can be obtained from (ψ^-, v^-) (respectively, (ψ^+, v^+)) by operating the substitution $w_0 \rightarrow w_0/2$ (respectively, $w_0 \rightarrow -w_0/2$) in equation (3.3).

3.2.3. Cycle periodicity

Both the layer transition and the glide equation are invariant by the transformation $(w_0, \psi) \mapsto (-w_0, -\psi)$. This can be seen as the consequence of the fact that the airspeed gain of flying upwind out of the slow layer is equal to that of flying downwind into the slow layer (this symmetry is particular to the Rayleigh problem: a finite thickness shear layer or a constraint on the average travel direction would break it).

Accordingly, the physical cycle (transition up \rightarrow wind layer glide \rightarrow transition down \rightarrow slow layer glide) can be subdivided into two equivalent subunits (transition \rightarrow glide) \rightarrow (transition \rightarrow glide), expanded below:

$$\dots (\psi^+, v^+)_{n-1} \xrightarrow{\text{glide}} \underbrace{(\psi^-, v^-)_n \xrightarrow{\text{transition}} (\psi^+, v^+)_n \xrightarrow{\text{glide}} (\psi^-, v^-)_{n+1}}_{\text{sub-unit } n} \dots$$

In a stationary cycle, the airspeed is periodic $v_{n+1} = v_n$ and the heading angle is anti-periodic $\psi_{n+1} = -\psi_n$. Therefore, the heading angle evolves by $\psi_{n+1}^- - \psi_n^+ = \psi_{n+1}^- + \psi_{n+1}^+$ over a glide phase. The evolution of airspeed and air-relative heading angle are sketched in figure 5.

3.2.4. Large glide ratio limit

Previous studies [5] have shown that the necessary wind speed w_0 tends to 0 as the glide ratio f tends to ∞ . Assuming $f \gg 1$ and $w_0 \ll 1$, the loss of airspeed during the glide phase can be approximated by Euler integration

$$\Delta v_{\text{glide}} \approx -\frac{v}{f\alpha} |\Delta\psi| \quad \text{with } \alpha = \sqrt{1 - 1/(c_L^2 v^4)} \quad (3.4)$$

(see electronic supplementary material, ST4 for a treatment with explicit residuals). For a stationary cycle, equation (3.3a) used twice (between ψ^- and ψ_0 and then between ψ^+ and ψ_0) yields $\Delta\psi = \psi^+ + \psi^- \approx 2\psi_0$. This can be interpreted as the heading in the middle of the shear layer is approximately the average of the headings just before and just after crossing. Similarly, equation (3.3b), gives

$$\Delta v_{\text{transition}} = v^+ - v^- \approx w_0 \sin \psi_0. \quad (3.5)$$

When the cycle is stationary, the airspeed loss during glides and airspeed gain during transitions must compensate

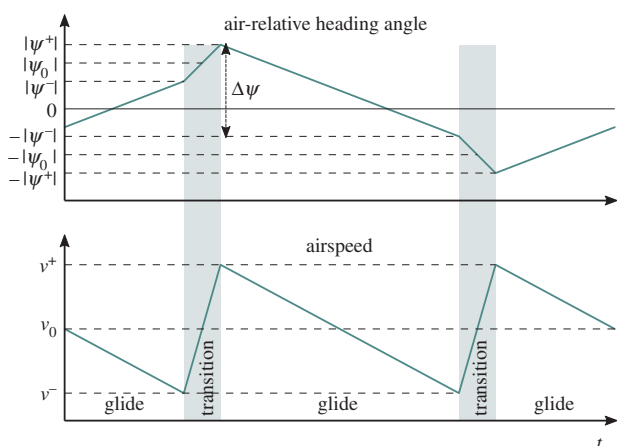


Figure 5. Sketch of the evolution of airspeed and air-relative heading angle over one dynamic soaring cycle, in the large glide ratio approximation. Following a glide phase in the boundary layer, the glider transitions into the wind layer, experiencing a shift of its air-related heading to port, as well as an airspeed boost. A glide phase in the wind layer ensues and is followed by a transition into the boundary layer which is associated to a shift of air-related heading to starboard and an airspeed boost. The cycle in this figure starts a quarter period earlier than in the right-hand side of figure 4. In the thin shear layer limit, airspeed has double periodicity and air-related heading has double anti-periodicity, such that the physical cycle may be divided into two equivalent sub-units.

each other. Equating loss and gain brings the equation for the average airspeed

$$\frac{v}{\sqrt{1 - 1/(c_L^2 v^4)}} = \frac{\sin \psi_0}{\psi_0} \frac{f}{2} w_0. \quad (3.6)$$

The minimum w_0, v pair

$$w^* = \frac{3^{3/4} \sqrt{2}}{c_L^{3/2}/c_D} \quad v^* = \frac{3^{1/4}}{\sqrt{c_L}} \quad (3.7)$$

is attained when the cardinal sine $\text{sinc}(\psi_0) \equiv \sin(\psi_0)/\psi_0$ is maximized, i.e. $\psi_0 \rightarrow 0$. The minimum wind w^* is smaller by a factor $\pi/2$, compared to when half-turns are required ($\psi_0 = \pi/2$). Note also that in the minimum-wind problem, the aerodynamic quantity of interest is the so-called coefficient of minimum power $(c_L^{3/2}/c_D)_{\max}$.

3.3. Comparison with recordings of wandering albatrosses and other numerical studies

The main characteristics of the numerical model are strikingly consistent with albatross flight data (figures 6 and 7), and a significant improvement over the half-turn description, especially given the uncertainty associated with the wind field. In particular, Sachs' low-wind recording is both in the low-end of reports of dynamically soaring wandering albatrosses, and within 10% of the prediction of our numerical model. Turn angles are consistent ($D \geq 102$, $p \leq 10^{-20}$, see electronic supplementary material, ST2) between the numerical model (65° – 100° , value for most likely conditions 80°), and Sachs' and Yonehara's albatross tracks (typically 50° – 70° in crosswind).

We also compared the model with studies based on a log-profile wind field [25,33] and they agree within 10% for key aspects of the soaring cycle such as turn angle and required wind intensity (figures 6 and 7). This suggests that the

dynamic soaring trajectory is robust to variations of the wind field, and that our two-parameter formulation in equation (2.1) is successful at capturing the main characteristics of dynamic soaring, even in attached flows, e.g. logarithmic profiles.

4. Discussion

While in dynamic soaring the energy extraction process has historically been explained as a sequence of half-turns, high-rate GPS recordings of wandering albatrosses in cross-wind flight show that they typically turn by approximately 50° – 70° , about a third of the half-turn (figures 2a and 6b). When the shear layer being exploited for dynamic soaring is thick, when compared with the characteristic length $\lambda = 2m/\rho S$, the minimum-wind (most energy-efficient) trajectory is indeed a succession of half-turns. When the shear layer is thin however, the minimum-wind trajectory is a succession of shallow arcs, forming a zigzagging path, as elongated as the shear layer is thin (figure 4). Similarly, our analytic model states that in thin shear layers, shallow arcs are energetically more efficient. In equations (3.7) and (4.2) below, we provide an analytic value for the minimum wind speed needed to sustain flight in the thin shear layer regime. As seen in figure 6, it predicts the thin shear layer limit of the numerical model and is smaller than previous studies by a factor $\pi/2$.

Wandering albatrosses exploit the shear layer just above the surface of the ocean, approximately 1–3 m thick. This is thin compared to $\lambda_{\text{albatross}} = 24$ m, suggesting that elongated trajectories are indeed energetically beneficial for them. For such a shear layer thickness, our numeric model predicts a turn amplitude of the minimum-wind trajectory between 65° and 100° , depending on the actual shear layer thickness and the glider's aerodynamic efficiency.

In practice, several factors not taken into account in the present models may influence the cycle frequency and shape, and cause variability in the dynamic soaring trajectory. The large albatross wingspan (3 m) implies a cost of rolling not taken into account in our point-mass model, as well as a constraint on its minimum vertical travel, both of which favour cycles of larger duration and amplitude. Waves influence the wind field through two mechanisms: wave propagation causes an updraft flow on their front sides, while wind–wave interactions influence the structure of the wind boundary layer. For instance, wind separation on the lee side of waves in a young sea state (when the wind is faster than the waves' phase speed) may result in a pocket of slow air as illustrated in figure 1a (see also [10]), with an influence on the shear layer thickness. It may be energetically beneficial for albatrosses to adapt their trajectory in order to synchronize with waves and exploit these features.

When the wind is plentiful, and the primary objective of staying aloft is easily attained, it is likely that albatrosses adapt their flight strategy in order to fulfil secondary objectives, such as choosing their beeline travel speed, reducing their overall control activity, reducing aerodynamic loads, exploring specific heights, travelling upwind, etc. For instance, phases when an albatross flies and remains at extreme low height without rolling may be slightly beneficial in terms of reduced drag due to ground effect; they also skew the overall beeline trajectory windward, as more time is spent

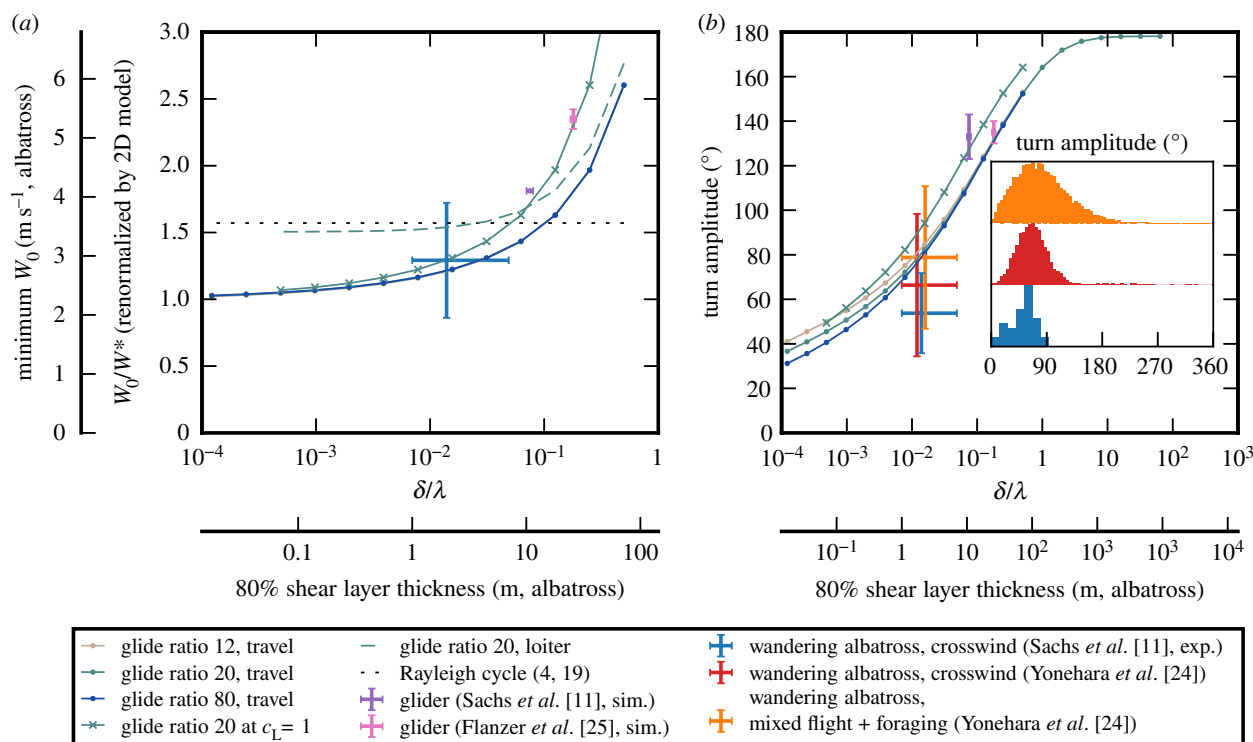


Figure 6. Minimum wind and turn amplitude of the travelling and loitering trajectories as a function of the shear layer thickness from our numerical model, for various glide ratios. Unless otherwise indicated, the maximum glide ratio is reached at $c_L = 0.5$. The model is compared with experimental (exp.) data of flying albatrosses from [11,24], and simulations (sim.) of dynamic soaring in a logarithmic wind field from [25,33]. (a) In the thin shear layer regime $\delta \rightarrow 0$, the wind required for the travelling trajectories converges to our two-dimensional model in equation (4.2). (b) Similarly, the turn amplitude decreases and the trajectories become straighter. The histogram insets represent the turning statistics of Sachs *et al.* [11], Yonehara *et al.* [24] albatross #4 and #2 from bottom to top. Yonehara's albatrosses are recorded over hundreds of kilometres. In crosswind, the recorded albatrosses typically turn by $50^\circ - 70^\circ$ while in the recorded mixed-flight the typical turn amplitude is 80° . Error bars represent the median turn ± 1 s.d.

in a slower flow. Overall, all these effects potentially influence the actual albatross trajectory in complex and intricate ways, and it is striking and surprising that despite changing conditions (in particular, wind relative direction and intensity and wave field), the turn amplitude of crosswind flight remains relatively constant across the datasets considered.

Despite the aforementioned variability, the following conclusion holds: for the albatross, finite turns are not the cause of energy extraction, but a consequence of shear layer thickness and the aforementioned effects. The half-turn picture with up- and downwind transitions is misleading, as it is suboptimal both energetically and for travel speed.

Below, we shed additional light on the rigorous analysis of the analytic model by qualitatively discussing three intuitive explanations of the exchanges at play in the thin shear layer dynamic soaring manoeuvre.

4.1. Airspeed loss and gain

Rayleigh's description of dynamic soaring, and our analytic model, both express the fact that in the thin shear layer regime, a dynamic soaring system gains airspeed each time it crosses the shear layer, and loses airspeed from drag when it flies in-between crossings. The airspeed gain upon crossing is approximately equal to the negative dot product between the wind and the glider's flight direction, i.e. $w_0 \sin \psi_0$, as shown in equation (3.5). For this airspeed gain to happen (figure 2b,c), the glider must turn by an amount $\Delta\psi \approx 2\psi_0$, which is associated (see equation (3.4)) to an airspeed loss due to drag of $(c_D/c_L)V/\sqrt{1 - V_c^2/(c_L^2 V^4)}|\Delta\psi|$. As such, the airspeed loss is proportional to the angle of turn.

Therefore, while the airspeed gain during a single transition is proportional to $\sin \psi_0$, the airspeed loss is proportional ψ_0 . The performance is driven by the ratio between gains and losses, which is proportional to $\sin(\psi_0)/\psi_0$, and maximized when $\psi_0 \rightarrow 0$. In the thin shear layer regime, frequent and small airspeed gains are more efficient than large and infrequent ones. This is visible in equation (3.6) relating airspeed, turn angle and wind intensity. Rewritten in its dimensional form (remember that

$V_c = \sqrt{mg/(\frac{1}{2}\rho S)}$), it becomes

$$\frac{V}{\sqrt{1 - V_c^2/(c_L^2 V^4)}} = \frac{\sin \psi_0}{\psi_0} \frac{c_L}{2c_D} W_0 \quad (4.1)$$

and the dimensional wind–airspeed relationship is

$$W^* = \frac{3^{3/4}\sqrt{2}}{c_L^{3/2}/c_D} V_c \quad \text{and} \quad V^* = \frac{3^{1/4}}{\sqrt{c_L}} V_c. \quad (4.2)$$

In practice, the sensitivity of equation (4.1) with respect to ψ_0 is small and equation (4.2) approximately holds even for finite angles of turn, because the cardinal sine ($\text{sinc}(\psi_0) \equiv \sin(\psi_0)/\psi_0$) is flat in the neighbourhood of 0. For instance, for 60° turns, $\text{sinc}(\psi_0) = 0.95$. In fact, even quarter-turns, for which $\text{sinc}(\psi_0) = 0.90$, are energetically much closer to the small turn limit $\text{sinc}(0) = 1$, than to the half-turn value $\text{sinc}(\psi_0) = 0.64$.

Conversely, when the shear layer is thick, the numeric analysis suggests that because crossing through it requires flying a comparatively large distance (and incurs large drag losses) anyway, maximizing the airspeed gain at each

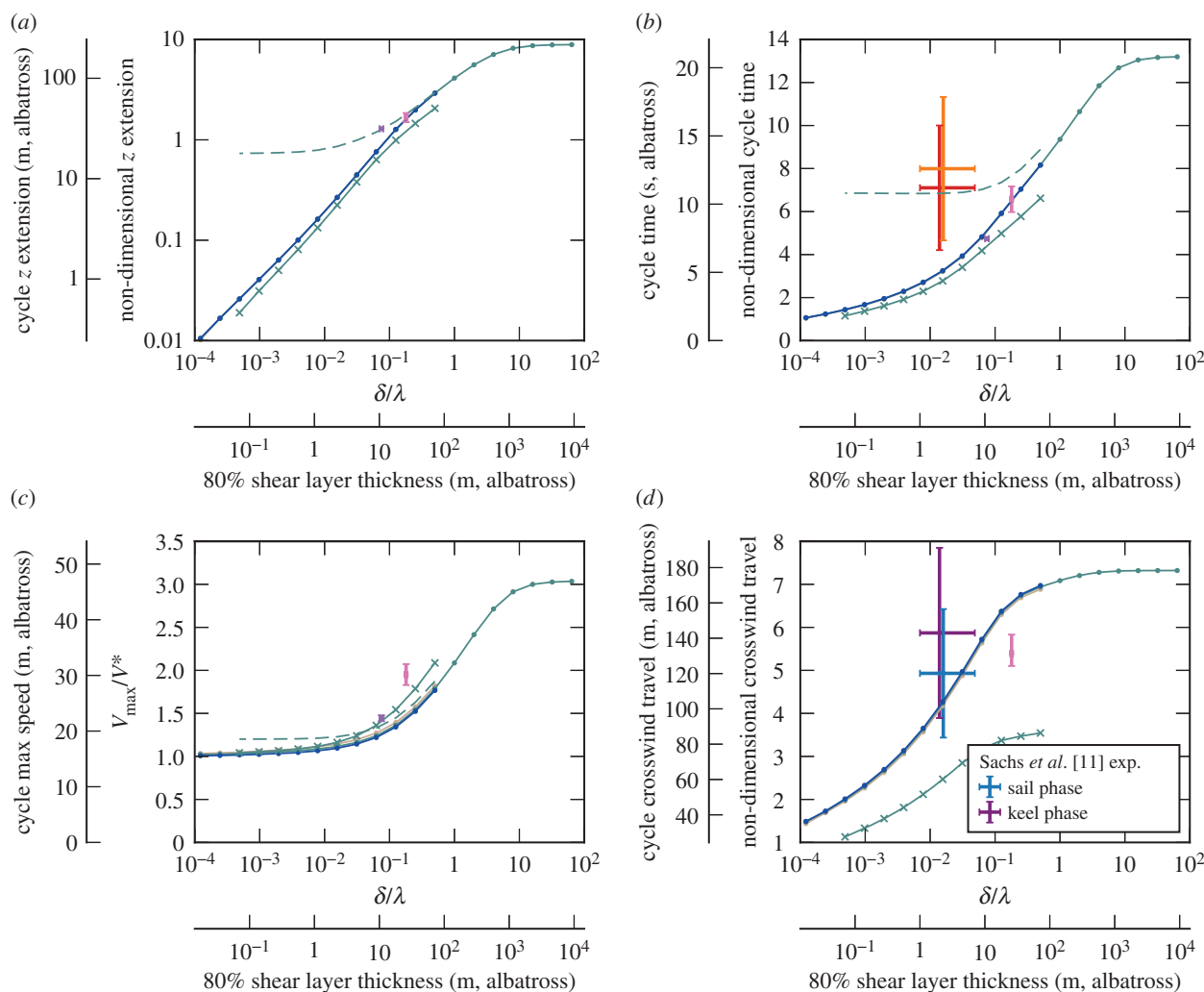


Figure 7. Characteristics of the minimum-wind cycle. Same legend as in figure 6. (a) Height separation between the lowest and highest point of the cycle. For thin shear layers the travelling trajectory is nearly two-dimensional. Note that the convergence rate is only about $z \sim \delta^{2/3}$. (b) Cycle duration. (c) Maximum airspeed attained during the cycle. (d) Crosswind travel during one cycle. The blue (respectively, purple) markers correspond to twice the length of the sail (respectively, keel) phase in figure 2a.

transition becomes relatively more important. Accordingly, when the shear layer is thick, the minimum-wind trajectory is composed of large-amplitude turns.

4.2. Shed vorticity and wake

For a qualitative description, consider the thin shear layer case when the trajectory and flows are approximately two-dimensional, as in the bottom of figure 2c. In this framework, the glider is nearly always at a large roll angle and as seen from above it resembles two-dimensional aerofoil. Successively, the glider enters a layer, performs a glide, and then leaves the layer as it transitions to the other one. Under the reasonable assumption that successive glide phases do not interact with each other, before the glider enters in a layer, the flow velocity is uniform at W_0 (wind layer) or 0 (slow boundary layer).

Because the foil generates lift, it carries bound vorticity with it. For instance in figure 2c, the glider is in the wind layer, and banked to starboard such that, as seen from above, the bound vorticity is clockwise. By Kelvin's circulation theorem, a vortex of equal intensity and opposite sign (anticlockwise in figure 2c) must have been shed where the glider entered the layer. After the glide phase, the glider

leaving the wind layer is a 'vanishing foil' [36], and its bound vorticity is shed into the flow.

Thus, as illustrated in figure 2c, the effect of the glider's passage is a pair of counter-rotating vortices shed in the flow, along a generally crosswind line. These vortex pairs constitute the signature of jets, which are directed upwind in the wind layer and downwind in the slow layer. The effect of these jets is an overall slowdown of air in the fast wind layer, and acceleration of air in the slow boundary layer. In other words, through dynamic soaring the glider transfers momentum between the wind layer and the boundary layer, which tends to reduce the overall speed difference between those two layers, and is associated with the flow losing kinetic energy.

Note that the definition of kinetic energy depends on the frame of reference. In the case of crosswind dynamic soaring, it is interesting to consider the system in the inertial frame of reference convected at the average velocity between the boundary layer and the wind layer, i.e. $W_0/2$. In this frame, the wind layer velocity is $W_0/2$ while the boundary layer velocity is $-W_0/2$. Therefore, both glide phases play very similar roles, with both jets tending to reduce the absolute value of the flow velocity in their respective layers. In fact, it is in this particular frame of reference that the analytic minimum wind trajectory is crosswind—it appears somehow downwind from an observer attached to Earth or the water surface.

4.3. Analogy with sailing

Dynamic soaring presents strong similarities to sailing: sailboats propel themselves by transferring momentum from the fast wind to the slow-moving ocean by means of two lifting surfaces, the sail and the keel. As pictured in figure 2c,d, the sail serves to extract momentum from the wind, thereby slowing it down, while the keel serves to inject that momentum to the water, thereby accelerating it. As such, the sail of a sailboat and an albatross flying in the wind layer both fulfil a 'sail functionality', while a sailboat's keel and an albatross flying in the boundary layer both fulfil a 'keel functionality'. As a consequence, the albatross can be viewed as a sequential, 'flying sailboat' with the two particularities that (i) it acts between the wind layer and the boundary layer rather than between the wind and water, and (ii) the sail and keel functions emerge from the dynamic soaring manoeuvre itself rather than from dedicated structural appendages as on a sailboat.

Finally, consider the sail of a sailboat, analysed in the Earth frame of reference. The lift force, responsible for extracting momentum from the wind, is by definition perpendicular to the local airflow. If the sail was going directly up- or downwind, the local airflow and Earth-related velocity would be aligned, the lift force and Earth-related velocity would be orthogonal, and therefore the power of the lift force $L \cdot U_{\text{Earth}}$ would be 0. Conversely, when the sail is going crosswind, there is a misalignment between the local airflow and Earth-related velocity which implies a non-zero dot product between lift and inertial velocity (a thrust force, figure 2c), which means extraction of power. Like the sailboat (figure 2d), the albatross extracts power in flight phases where it is crosswind rather than directly up- or downwind.

5. Conclusion

The conceptual framework presented in this paper improves the general understanding of dynamic soaring with a low-order and yet accurate model, and points to the potentially major role played by wind separation behind waves in albatross flight. This has applications for refining the characterization and prediction of the albatross' habitat in a changing climate. In the quest for a robotic, bioinspired albatross, equation (4.2) may well constitute the fundamental design guideline, while understanding the key roles of shear layer thickness and turn amplitude paves the way to robust and scalable learning algorithms for online trajectory planning and control in robotic dynamic soaring applications.

Data accessibility. This article has no additional data.

Author's contributions. G.D.B. conceived the mechanistic model and carried the analyses. M.S.T. suggested the general field of study. J.-J.E.S. supervised the study. M.S.T. and J.-J.E.S. helped refine the analyses. G.D.B., M.S.T. and J.-J.E.S. wrote the manuscript.

Competing interests. The authors declare no competing interests.

Funding. This research was supported in part by a Fulbright Science and Technology fellowship, a Prof. Amar G. Bose research grant, a Link Foundation Ocean Engineering & Instrumentation fellowship as well as from SMART, the Singapore-MIT Alliance for Research and Technology, within the CENSAM programme.

Acknowledgments. We thank J. Izraelevitz and L. Mendelson, as well as P. Beynet, L. Deike, A. Demarais, E. Ferenczi, J. Schulmeister, A. Teffer, A. Xibu, and the reviewers, including G. Bohrer and T. Katzner, for stimulating discussions and feedback. We also wish to acknowledge the authors of [11,24], namely F. Bonadonna, Y. Goto, A. P. Nesterova, G. Sachs, K. Sato, J. Traugott, Y. Watanuki, H. Weimerskirch, K. Yoda, Y. Yonehara and L. C. Young for their enabling work in publishing the characteristics of wandering albatross flights. We thank Ewen Bell for kindly providing the albatross photograph.

References

- Sachs G, Traugott J, Nesterova AP, Dell'Omo G, Kümmeth F, Heidrich W, Vyssotski AL, Bonadonna F. 2012 Flying at no mechanical energy cost: disclosing the secret of wandering albatrosses. *PLoS ONE* **7**, e41449. (doi:10.1371/journal.pone.0041449)
- Catry P, Phillips RA, Croxall JP. 2004 Sustained fast travel by a gray-headed albatross (*Thalassarche chrysostoma*) riding an Antarctic storm. *Auk* **121**, 1208–1213. (doi:10.1642/0004-8038(2004)121[1208:SFTBAG]2.0.CO;2)
- Weimerskirch H, Guionnet T, Martin J, Shaffer SA, Costa DP. 2000 Fast and fuel efficient? Optimal use of wind by flying albatrosses. *Proc. R. Soc. Lond. B* **267**, 1869–1874. (doi:10.1098/rspb.2000.1223)
- Sachs G, da Costa O. 2006 Dynamic soaring in altitude region below jet streams. In *AIAA Guidance, Navigation, and Control Conference*, 21–24 August, Keystone, Colorado.
- Bower G. 2011 Boundary layer dynamic soaring for autonomous aircraft: design and validation. PhD thesis, Stanford University, Stanford, CA, USA.
- Langelaan JW, Roy N. 2009 Enabling new missions for robotic aircraft. *Science* **326**, 1642–1645. (doi:10.1126/science.1182497)
- Weimerskirch H, Louzao M, de Grissac S, Delord K. 2012 Changes in wind pattern alter albatross distribution and life-history traits. *Science* **335**, 211–214. (doi:10.1126/science.1210270)
- Nevitt GA, Losekoot M, Weimerskirch H. 2008 Evidence for olfactory search in wandering albatross, *Diomedea exulans*. *Proc. Natl Acad. Sci. USA* **105**, 4576–4581. (doi:10.1073/pnas.0709047105)
- Rayleigh JWS. 1883 The soaring of birds. *Nature* **27**, 534–535. (doi:10.1038/027534a0)
- Buckley MP, Veron F. 2016 Structure of the airflow above surface waves. *J. Phys. Oceanogr.* **46**, 1377–1397. (doi:10.1175/JPO-D-15-0135.1)
- Sachs G, Traugott J, Nesterova AP, Bonadonna F. 2013 Experimental verification of dynamic soaring in albatrosses. *J. Exp. Biol.* **216**, 4222–4232. (doi:10.1242/jeb.085209)
- Richardson PL. 2011 How do albatrosses fly around the world without flapping their wings? *Prog. Oceanogr.* **88**, 46–58. (doi:10.1016/j.pocean.2010.08.001)
- Jameson WS. 1958 *The wandering albatross*. London, UK: Rupert Hart-Davis.
- Cone CD. 1964 A mathematical analysis of the dynamic soaring flight of the albatross with ecological interpretations. Special scientific report (Virginia Institute of Marine Science); no. 50. Gloucester Point, VA: Virginia Institute of Marine Science, College of William and Mary. (doi:10.21220/VSP88C)
- Wood CJ. 1973 The flight of albatrosses (a computer simulation). *Ibis* **115**, 244–256. (doi:10.1111/j.1474-919X.1973.tb02640.x)
- Boslough MBE. 2002 Autonomous dynamic soaring platform for distributed mobile sensor arrays. Technical report. Albuquerque, NM: Sandia National Laboratories.
- Lissaman P. 2005 Wind energy extraction by birds and flight vehicles. In *AIAA Guidance, Navigation, and Control Conference*, 10–13 January, Reno, Nevada.
- Barate R, Doncieux S, Meyer J-A. 2006 Design of a bio-inspired controller for dynamic soaring in a simulated unmanned aerial vehicle. *Bioinspir. Biomim.* **1**, 76–88. (doi:10.1088/1748-3182/1/3/002)
- Denny M. 2009 Dynamic soaring: aerodynamics for albatrosses. *Eur. J. Phys.* **30**, 75–84. (doi:10.1088/0143-0807/30/1/008)
- Lawrance NRJ. 2011 Autonomous soaring flight for unmanned aerial vehicles. PhD thesis, University of Sydney, New South Wales, Australia.
- Bonnin V, Toomer CC. 2013 Energy-harvesting mechanisms for UAV flight by dynamic soaring. In

- AIAA Guidance, Navigation, and Control Conference, 19–22 August, Boston, MA.
22. Bird JJ, Langelaan JW, Montella C, Spletzer JR, Grenestedt JL. 2014 Closing the loop in dynamic soaring. In *AIAA Guidance, Navigation, and Control Conference*, 13–17 January, National Harbor, Maryland.
 23. Gao X-Z, Hou Z-X, Guo Z, Chen X-Q. 2015 Energy extraction from wind shear: reviews of dynamic soaring. *Proc. Inst. Mech. Eng. [G]* **229**, 2336–2348. (doi:10.1177/0954410015572267)
 24. Yonehara Y, Goto Y, Yoda K, Watanuki Y, Young LC, Weimerskirch H, Bost C, Sato K. 2016 Data from: Flight paths of seabirds soaring over the ocean surface enable measurement of fine-scale wind speed and direction. Dryad Digital Depository. (doi:10.5061/dryad.3pb86)
 25. Flanzer TC, Bunge RA, Kroo IM. 2012 Efficient six degree of freedom aircraft trajectory optimization with application to dynamic soaring. In *AIAA Aviation Technology, Integration, and Operations Conference*, 17–19 September, Indianapolis, Indiana.
 26. Deittert M, Richards A, Toomer CA, Pipe A. 2009 Engineless unmanned aerial vehicle propulsion by dynamic soaring. *J. Guid. Control Dyn.* **32**, 1446–1457. (doi:10.2514/1.43270)
 27. Pennycuik CJ. 2002 Gust soaring as a basis for the flight of petrels and albatrosses (Procellariiformes). *Avian Sci.* **2**, 1–12.
 28. Pennycuik CJ. 2008 *Modelling the flying bird*, vol. 5. Amsterdam, The Netherlands: Elsevier.
 29. Phillips WH. 1975 Propulsive effects due to flight through turbulence. *J. Aircr.* **12**, 624–626. (doi:10.2514/3.44480)
 30. Patel CK, Lee H-T, Kroo IM. 2008 Extracting energy from atmospheric turbulence. In *XXIX OSTIV Congress*, 6–13 August, Lisse-Berlin, Germany.
 31. Zhao YJ. 2004 Optimal patterns of glider dynamic soaring. *Optimal Control Appl. Methods* **25**, 67–89. (doi:10.1002/oca.739)
 32. Pennycuik CJ. 1982 The flight of petrels and albatrosses (Procellariiformes), observed in South Georgia and its vicinity. *Phil. Trans. R. Soc. Lond. B* **300**, 75–106. (doi:10.1098/rstb.1982.0158)
 33. Sachs G. 1993 Minimaler Windbedarf für den dynamischen Segelflug der Albatrosse. *J. für Ornithologie* **134**, 435–445. (doi:10.1007/BF01639834)
 34. Gent PR, Taylor PA. 1977 A note on ‘separation’ over short wind waves. *Boundary Layer Meteorol.* **11**, 65–87. (doi:10.1007/BF00221825)
 35. Yonehara Y, Goto Y, Yoda K, Watanuki Y, Young LC, Weimerskirch H, Sato K. 2016 Flight paths of seabirds soaring over the ocean surface enable measurement of fine-scale wind speed and direction. *Proc. Natl Acad. Sci. USA* **113**, 9039–9044. (doi:10.1073/pnas.1523853113)
 36. Steele SC, Dahl JM, Weymouth GD, Triantafyllou MS. 2016 Shape of retracting foils that model morphing bodies controls shed energy and wake structure. *J. Fluid Mech.* **805**, 355–383. (doi:10.1017/jfm.2016.553)